

Banner appropriate to article type will appear here in typeset article

# Surface instabilities in laminar compressible boundary layers with sublimation

Blaine Vollmer<sup>1</sup>†, Alberto Padovan,<sup>1</sup> and Daniel J. Bodony<sup>1</sup>

<sup>1</sup>Department of Aerospace Engineering, University of Illinois Urbana-Champaign, Urbana, IL 61801, USA

(Received xx; revised xx; accepted xx)

Surface patterns on ablating materials are observed in high-speed ground and flight tests, but the mechanisms behind their formation are not known. In this paper, the origin of surface patterns is investigated via a local linear stability analysis of compressible laminar boundary layers over a flat camphor plate. The effects of sublimation and conjugate heat transfer are included both on the baseflow and the linear fluctuations. This framework identifies one mode that fully characterizes the stability of the surface, which becomes unstable when the wall temperature exceeds that of an adiabatic wall,  $T_{ad}$ . These findings are consistent with experimental observations, where laminar flow conditions at adiabatic wall temperatures are found to be stable. The analysis also reveals that the nature of this surface mode varies as a function of the oblique angle  $\psi = \tan^{-1} \beta/\alpha$ , where  $\alpha$  and  $\beta$  are the streamwise and spanwise wavenumbers. Specifically, for baseflow temperatures below  $\approx 1.15 T_{ad}$ , the surface mode is most unstable at  $\psi = 0$ . Conversely, above  $\approx 1.15 T_{ad}$  the surface is most unstable near the sonic angle  $\psi_s = \cos^{-1}(1/M_e)$ , which is the angle at which the normal Mach number equals one. Finally, a critical wavenumber is identified (i.e., one at which the temporal growth rate reaches a maximum) that is in good agreement with available experimental observations of turbulent flows.

**Key words:** Compressible boundary layers, Supersonic flow, Flow-structure interactions

## 1. Introduction

Ablating thermal protection systems are used to shield hypersonic vehicles from the thermal loads experienced during flight. As the surface ablates, the vehicle surface changes shape and can develop surface patterns. Both flight and ground testing have shown that ablating materials can exhibit macro-scale surface patterns of different types including streamwise grooves, wedges, crosshatching, and scallops (Grabow & White 1975). These patterns can occur for melting, sublimating, and charring processes, and are observed on a wide range of materials including phenolics, plastics, and wood (Stock & Ginoux 1973). Examples of sublimation-induced surface patterns are shown in Figure 1. The crosshatched surface (rightmost panel in Figure 1) has received the most attention in the literature as it consists

† Email address for correspondence: blaine2@illinois.edu

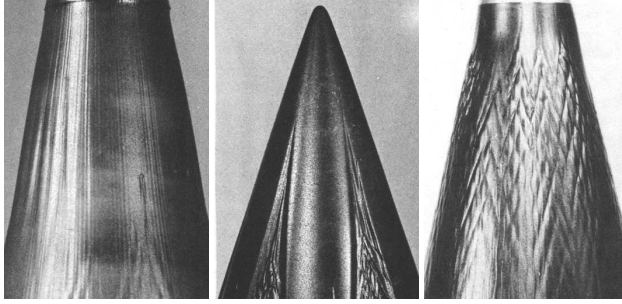


Figure 1: Ablation patterns showing streamwise grooves (left), turbulent wedges (middle), and crosshatching (right). Images taken from Figure 1 of Stock & Goddard (1973).

of a regular pattern of spatially-periodic raised or recessed rhomboidal patterns. The pattern angles are shown to be well correlated with the local Mach angle (Swigart 1974).

While crosshatching has been observed only for supersonic turbulent flows, laminar instabilities may exist under conditions that have not yet been explored, namely hot wall conditions with  $T_w > T_{ad}$ , where  $T_w$  is the wall temperature and  $T_{ad}$  is the adiabatic wall temperature. In experiments studying ablation surface patterns, the freestream stagnation temperatures are typically much greater than the sample surface temperature at the start of the experiment, which creates an initial cold-wall condition  $T_w < T_{ad}$ . Even if the stagnation temperature is near the initial material temperature, the runtime required to produce crosshatching patterns is such that the material reaches the steady adiabatic condition prior to crosshatching formation (Stock & Goddard 1973). The effects of hot walls could be investigated by heating part of the material that is not exposed to the flow to create an equilibrium temperature greater than the adiabatic condition.

The mechanism by which surface patterns emerge on an ablating material is not known. Proposed crosshatching mechanisms were reviewed by Swigart (1974), including differential ablation, inelastic deformation, and liquid layer models. Several of the reviewed mechanisms have the potential to explain the formation of crosshatching, but further investigation is required. The present work focuses on differential ablation of pure sublimators. The framework and methodology may be readily extended to porous ablators and inelastic deformation models to study additional surface instability mechanisms.

The differential ablation mechanism was studied by Lees *et al.* (1972), where a simplified linear stability analysis of the coupled fluid-sublimation system was performed on a mean turbulent baseflow. The simplifying assumptions include steady fluid perturbations, isothermal boundary conditions, single-species chemistry, and non-sublimating baseflows. The use of an isothermal wall boundary condition implies that sublimation is not appropriately accounted for. In this case, the sublimation rate is found by the energy balance that produces an isothermal wall. The linear analysis by Lees *et al.* (1972) identified an oblique surface mode as the most unstable, demonstrating that differential ablation can produce surface instabilities. However, Swigart (1974) reported another result from Lane and Ruger (unpublished), that contradicted the results of Lees *et al.* (1972) and showed no such instability. The Lane and Ruger results do not appear to be published, and it is still unknown whether differential ablation is a viable mechanism for surface patterns.

This paper presents a more complete formulation of differential ablation stability than Lees *et al.* (1972) by considering the full unsteady system with sublimation models and conjugate heat transfer within the solid. The surface stability of supersonic laminar flow over a flat camphor surface is analyzed at varying wall temperature ratios. The surface is found to be unstable for wall temperatures sufficiently greater than the adiabatic temperature,

$T_w > 1.07 T_{ad}$ , and stable otherwise. These findings are consistent with experimental observations where patterns do not develop for laminar cold-wall conditions, and the results predict that hot-wall experiments, which to our knowledge have not yet been performed, will produce a laminar instability. The governing equations for the fluid, solid, and interface sublimation are presented in Section 2. Section 3 presents the linearization procedure, and Section 4 presents the results.

## 2. Governing Equations and Material Models

### 2.1. Fluid

The fluid is governed by the frozen-flow multi-species compressible Navier-Stokes equations, written in compact form as

$$\frac{\partial \mathbf{Q}}{\partial t} + \frac{\partial \mathbf{F}_i}{\partial x_i} + \frac{\partial \mathbf{G}_i}{\partial x_i} = 0, \quad (2.1)$$

where  $\mathbf{Q}$  is the vector of conservative flow variables,  $\mathbf{F}$  denotes the inviscid fluxes and  $\mathbf{G}$  denotes the viscous fluxes,

$$\mathbf{Q} = \begin{bmatrix} \rho \\ \rho u_1 \\ \rho u_2 \\ \rho u_3 \\ \rho E \\ \rho_1 \\ \vdots \\ \rho_{n-1} \end{bmatrix}, \quad \mathbf{F}_i = \begin{bmatrix} \rho u_i \\ \rho u_1 u_i + p \delta_{1i} \\ \rho u_2 u_i + p \delta_{2i} \\ \rho u_3 u_i + p \delta_{3i} \\ (\rho E + p) u_i \\ \rho_1 u_i \\ \vdots \\ \rho_{n-1} u_i \end{bmatrix}, \quad \mathbf{G}_i = \begin{bmatrix} 0 \\ \tau_{1i} \\ \tau_{2i} \\ \tau_{3i} \\ u_j \tau_{ij} + q_i \\ \rho_1 w_{1i} \\ \vdots \\ \rho_{n-1} w_{(n-1)i} \end{bmatrix}. \quad (2.2)$$

Here,  $\rho$  is density,  $u_i$  are the Cartesian velocity components,  $E$  is the total energy,  $p$  is the pressure, and  $\rho_k$  and  $w_{ki}$  are mass-density and  $i$ th velocity for each chemical species  $k \in \{1, 2, \dots, n\}$ . The viscous stress tensor  $\tau_{ij}$ , heat-flux vector  $q_i$ , and species velocities are defined as

$$\tau_{ij} = \mu \left( \frac{\partial u_i}{\partial x_j} + \frac{\partial u_j}{\partial x_i} \right) + \lambda \frac{\partial u_i}{\partial x_i} \delta_{ij}, \quad q_i = \kappa \frac{\partial T}{\partial x_i} + \sum_{k=1}^n \rho_k h_k w_{ki}, \quad w_{ki} = -\frac{D_k}{c_k} \frac{\partial c_k}{\partial x_i} \quad (2.3)$$

where  $T$  is the fluid temperature,  $h_k$  is the species enthalpy, and  $c_k = \rho_k / \rho$  is the species mass fraction. The total energy per unit volume is given by

$$\rho E = \frac{p}{\gamma - 1} + \frac{1}{2} \rho \sum_{i=1}^3 u_i^2 + \sum_{k=1}^n \rho_k h_k^0 \quad (2.4)$$

where  $h_k^0$  is the enthalpy of formation and the ideal gas law is used for the mixture.

The transport coefficients ( $\mu_k$ ,  $\kappa_k$ , and  $D_k$ ) for a single species are given by kinetic theory (Hirschfelder *et al.* 1964). The mixture transport coefficients are found using the Wilke mixing rule with Eucken correction for conductivity. Details are given in Chapter 10 of Dorrance (1962). The collision integrals for the kinetic theory are evaluated using the high-order curve fit provided by Kim & Monroe (2014).

## 2.2. Solid

For the solid phase, a non-porous sublimator comprised of a single material with spatially-homogeneous isotropic thermal conductivity is considered. The solid is governed by the heat equation

$$\frac{\partial T_s}{\partial t} = \alpha_s \nabla^2 T_s, \quad (2.5)$$

where  $T_s$  is the temperature of the solid and  $\alpha_s$  the thermal diffusivity.

## 2.3. Interface

The interface between the fluid and sublimator is governed by mass and energy balances across the interface. These interface conditions can be derived formally from the governing equations on either side of the interface as done by Padovan *et al.* (2024). For an  $x_2$ -normal interface that does not accumulate mass, the interface conditions for mass conservation reduce to

$$(\rho_k v)_f + (\rho_k w_{k2})_f = \dot{m}_k, \quad (2.6)$$

where  $v_f = u_{2,f}$  is the vertical velocity component at the wall and  $\dot{m}_k$  is the species mass flux produced by the surface reaction. Subscript  $f$  refers to the external fluid. Summing over all species we find

$$\dot{m} = (\rho v)_f. \quad (2.7)$$

Similarly, the surface energy balance gives:

$$\left(-\kappa \frac{\partial T}{\partial y}\right)_f + (\rho v h)_f + \left(\sum_{k=1}^n \rho_k w_{k2} h_k\right)_f = \left(-\kappa \frac{\partial T}{\partial y}\right)_s + \dot{m} h_s \quad (2.8)$$

where  $h_s$  is the enthalpy of the solid sublimator, which accounts for surface reactions. For a binary mixture, with  $k = 1$  as the sublimator, this can be simplified to:

$$\left(-\kappa \frac{\partial T}{\partial y}\right)_f = \left(-\kappa \frac{\partial T}{\partial y}\right)_s - \dot{m} h_{sg} \quad (2.9)$$

where  $h_{sg}$  is the enthalpy of sublimation (solid to gas). The rate of surface recession is found by the rate of mass lost to sublimation

$$\dot{m} = -\rho_s v_s, \quad (2.10)$$

where  $\rho_s$  is the density of the solid and  $v_s$  is the velocity of the surface. For sublimating surfaces the Knudsen-Langmuir model is used in combination with the Clausius-Clapeyron relation for vapor pressure using the triple point:

$$\dot{m} = a_1 \frac{p_1^{sat} - p_1}{\sqrt{2\pi R_1 T_w}}, \quad \ln\left(\frac{p_1^{sat}}{p_{TP,1}}\right) = \frac{h_{sg}}{R_1} \left(\frac{1}{T_{TP,1}} - \frac{1}{T_w}\right) \quad (2.11)$$

where  $a_1$  is the accommodation coefficient and  $p_1$  is the partial pressure of the sublimating material. The superscript  $[]^{sat}$  refers to the saturation pressure, and the subscript  $[]_{TP}$  refers to the triple point.

### 2.3.1. Receding Surface

The governing equations are applied on the uniformly receding baseflow coordinate system, while perturbations to the surface are handled by linearized boundary conditions. The governing equations are transformed from the stationary reference frame  $x_i$  to a coordinate

system translating with the receding surface,  $\hat{x}_i$ . The time derivative in (2.1) transforms to

$$\left. \frac{\partial Q}{\partial t} \right|_{x_i} = \left. \frac{\partial Q}{\partial t} \right|_{\hat{x}_i} - v_s \frac{\partial Q}{\partial x_2}, \quad (2.12)$$

where  $v_s$  is the surface velocity in the vertical direction,  $x_2$ . Since  $v_s$  is constant for the uniformly receding baseflow, the moving coordinate term is combined with the convective fluxes to convert the  $u_2$  velocity to the relative velocity  $u_2 - v_s$ . Combining Equations (2.7) and (2.10) gives

$$v_f = -v_s (\rho_s / \rho_f + 1) \quad (2.13)$$

where  $\rho_f$  and  $v_f$  are the fluid density and velocity at the wall. Sublimators typically have a density much larger than the fluid such that  $\rho_s \gg \rho_f$ , which gives  $v_f \gg v_s$ . Therefore, the relative velocity terms can be neglected.

Equation (2.5) for the solid is transformed similarly:

$$\frac{\partial T_s}{\partial t} - v_s \frac{\partial T_s}{\partial x_2} = \alpha_s \nabla^2 T_s \quad (2.14)$$

No simplifying assumption is made for the solid to remove the surface velocity.

### 3. Linearization

The governing equations are linearized about a time-invariant parallel baseflow. In general, a given quantity  $\phi(x_i, t)$  is represented as

$$\phi(x_i, t) = \bar{\phi}(x_i) + \phi'(x_i, t), \quad (3.1)$$

where  $\bar{\phi}$  denotes the baseflow and  $\phi'(x_i, t)$  is a fluctuation. Here, we re-label the Cartesian coordinate system  $x_i = (x_1, x_2, x_3)$  to  $x_i = (x, y, z)$  for notational convenience. For the local stability analysis considered herein, the baseflow depends only on  $y$ , while the fluctuations take the form

$$\phi'(x_i, t) = \hat{\phi}(y) e^{i(\alpha x + \beta z - \omega t)}, \quad (3.2)$$

where  $\alpha$  and  $\beta$  are the wavenumbers in the streamwise and spanwise directions, respectively, and  $\omega$  is the frequency.

#### 3.1. Fluid

The linearization and modal ansatz are applied to the governing fluid equations (2.1) to obtain the local linear system

$$-i\omega \hat{q} = \tilde{A}(\bar{Q}, \alpha, \beta) \hat{q}, \quad (3.3)$$

where  $\tilde{A}$  is the linearized Jacobian. In this work the Jacobian is extracted from a nonlinear solver using a second-order Fréchet derivative. The solver has been verified against spatial boundary layer stability with blowing (Ghaffari *et al.* 2010), and against coupled non-linear fluid-ablation solvers for steady wavy walls.

##### 3.1.1. Baseflow

The baseflow is a self-similar compressible boundary layer with a non-reacting binary gas mixture. The equations are provided by Lysenko *et al.* (2021) and are repeated here for completeness. In particular,

$$\frac{d}{dy} \left( \mu \frac{dU}{dy} \right) + F \frac{dU}{dy} = 0, \quad \frac{dq}{dy} = F \frac{dh}{dy} + (\gamma_e - 1) M_e^2 \mu \left( \frac{dU}{dy} \right), \quad \frac{dj_1}{dy} = F \frac{dc_1}{dy} \quad (3.4)$$

where  $2\frac{dF}{dy} = \rho U$ ,  $q = \kappa\frac{dT}{dy} + j_1(h_1 - h_2)$  and  $j_1 = -\rho D_{12}\frac{dc_1}{dy}$ . The equations have been non-dimensionalized by the boundary layer edge quantities, with the Blasius length scale as the reference length  $\delta_{Bl} = \sqrt{x\mu_e/U_e\rho_e}$ . The slow-recession assumption discussed in Section 2.3.1 is present in these equations. The boundary conditions are found from the no-slip wall and the surface balances from Equations (2.7) and (2.8). With  $c_1$  representing the sublimating species mass fraction, the surface boundary conditions in non-dimensional form are:

$$U(0) = 0, \quad F(0) = -f_w = \frac{(\rho v)_f Re}{\rho_e u_e} \\ f_w h_{sg} + \left(-\kappa\frac{dT}{dy}\right)_f = \left(-\kappa\frac{dT}{dy}\right)_s, \quad f_w(1 - c_{1,w}) = -\rho_w D_{12,w}\frac{dc_1}{dy}\Big|_w, \quad (3.5)$$

where  $Re = \rho_e u_e \delta_{Bl} / \mu_e$ . The far-field conditions are  $U(\infty) \rightarrow 1$ ,  $T(\infty) \rightarrow 1$ , and  $c_1(\infty) \rightarrow 0$ . The equations are solved using a shooting method with iterations on the undetermined wall boundary conditions.

### 3.1.2. Boundary Conditions

Since the governing equations are solved on the nominally receding surface  $\bar{v}_s$ , the effects of perturbations to the surface resulting from  $v'_s$  must be accounted for. Taking the surface position to be at  $y = \eta'$ , where the nominal surface is at  $y = 0$ , a first-order Taylor expansion gives

$$\phi(\eta') = \bar{\phi}(0) + \phi'(0) + \frac{\partial \bar{\phi}}{\partial y}\Big|_0 \eta'. \quad (3.6)$$

This technique is applied to the wall boundary conditions, where  $u(\eta') = w(\eta') = 0$ , and  $v'(\eta') = -\dot{m}'/\rho_s$ . The temperature condition is obtained by the surface energy balance, including conjugate heat transfer with the solid. The same expansion procedure applies to gradients, which are used for enforcing the diffusion and heat flux conditions. This method of applying boundary conditions to the nominal surface position by linear expansion has been used on similar problems (Lees *et al.* 1972; Lekoudis *et al.* 1976).

## 3.2. Solid

The linearization and modal ansatz are applied to the solid equation (2.14), giving:

$$\frac{d^2 \hat{T}_s}{dy^2} + \frac{\bar{v}_s}{\alpha_s} \frac{d\hat{T}_s}{dy} + \left(\frac{i\omega}{\alpha_s} - \chi^2\right) \hat{T}_s = 0 \quad (3.7)$$

where  $\chi^2 = \alpha^2 + \beta^2$ . This is a second-order ordinary differential equation with constant coefficients. The analytical solution is:

$$\hat{T}_s = c_1 e^{m_1 y} + c_2 e^{m_2 y}, \quad m_{1,2} = \frac{1}{2} \left[ -\frac{\bar{v}_s}{\alpha_s} \pm \sqrt{\left(\frac{\bar{v}_s}{\alpha_s}\right)^2 - 4\left(\frac{i\omega}{\alpha_s} - \chi^2\right)} \right] := q \pm r \quad (3.8)$$

Considering a solid of thickness  $h$ , an isothermal far-field boundary condition at  $y = -h$  gives:

$$\frac{d\hat{T}_s}{dy}(\hat{\eta}) = \left( q + \frac{r}{\tanh(rh)} \right) \hat{T}_s(\hat{\eta}). \quad (3.9)$$

The total solid temperature gradient on the deformed surface is obtained using the expansion in (3.6):

$$\frac{dT_s}{dy}(\eta') = \left( \frac{d\bar{T}_s}{dy}(0) + \frac{d^2\bar{T}_s}{dy^2}\Big|_0 \eta' \right) + \left( q + \frac{r}{\tanh(rh)} \right) \left[ T_s(\eta') - \bar{T}_s(0) - \frac{d\bar{T}_s}{dy}\Big|_0 \eta' \right] \quad (3.10)$$

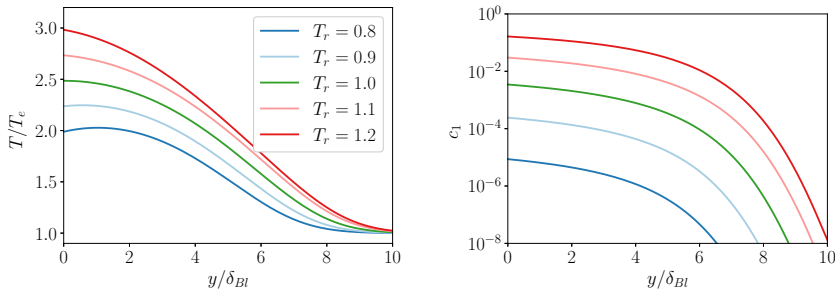


Figure 2: Self-similar baseflows with binary sublimation of camphor

### 3.2.1. Baseflow

Evaluation of (3.10) requires the first and second derivatives of  $\overline{T}_s$ . For a baseflow with an isothermal wall condition, the surface temperature gradients in the solid are found from the energy balance in (2.8) and steady solution from (2.14).

### 3.2.2. Boundary Conditions

The analytical boundary condition for  $d\hat{T}_s/dy$  given by (3.9) would lead to a nonlinear eigenvalue problem, where the eigenvalues are nonlinear functions of  $\alpha$ ,  $\beta$  and  $\omega$ . To simplify, a quasi-steady assumption is made where the solid response occurs much faster than the surface response, and the solid is approximately at a steady-state. Consequently, both  $\overline{v}_s/\alpha_s$  and  $\omega/\alpha_s$  are assumed much smaller than  $\chi$ , and taking  $h \rightarrow \infty$ , (3.9) simplifies to

$$\frac{d\hat{T}_s}{dy}(\hat{\eta}) = \chi \hat{T}_s(\hat{\eta}). \quad (3.11)$$

This boundary condition is now linear for a fixed oblique angle,  $\psi$ , as  $\chi = \alpha \sqrt{1 + \tan^2(\psi)}$ .

## 4. Results

Self-similar baseflows of a binary mixture boundary layer over a sublimating surface are computed for a range of freestream and wall temperature conditions. The freestream conditions considered are  $M = [2, 3, 4]$ ,  $Re = [500, 785, 1000, 10000]$ ,  $T_0 = [293, 400, 500]$  K, and  $p_0 = [0.1, 1, 10]$  bar. The stability results from all freestream conditions were qualitatively similar and only the results from  $M = 3$ ,  $Re = 785$ ,  $T_0 = 293$  K, and  $p_0 = 1$  bar are presented here. The wall temperature is chosen relative to the adiabatic temperature,  $T_{ad}$ , which is defined as the temperature at which the solid interface is adiabatic,  $d\overline{T}_s/dy = 0$ . The wall temperature ratio is then defined as  $T_r = T_w/T_{ad}$ . The sublimating material is camphor ( $C_{10}H_{16}O$ ) with molar mass  $MW = 152.23$  g/mol. The relevant properties of camphor were presented in Zibitsker *et al.* (2024) and are repeated here for completeness. The solid properties are  $\rho_s = 990$  kg/m<sup>3</sup>,  $\kappa_s = 0.2$  W/m · K, and  $c_{p,s} = 271.2$  J/mol · K. The vapor and transport properties are  $T_{TP} = 453.1$  K,  $p_{TP} = 0.514$  bar,  $\sigma = 6.87$  Å,  $\epsilon/k_B = 562$  K, and  $c_{p,g} = 192$  kg/m<sup>3</sup>. The specific heat of the gas is treated as constant and was obtained from the NASA-7 polynomial in Zibitsker *et al.* (2024) at  $T = 300$  K. The accommodation coefficient is  $a_1 = 0.18$ , and the enthalpy of sublimation is  $h_{sg} = 51.9$  kJ/mol · K.

Baseflow temperature and mass fraction profiles are shown in Figure 2 for wall temperatures ratios from  $T_r = 0.8 - 1.2$ . The profiles in Figure 2 show that for increasing wall temperature, the boundary layer thickness increases due to sublimation blowing. The amount

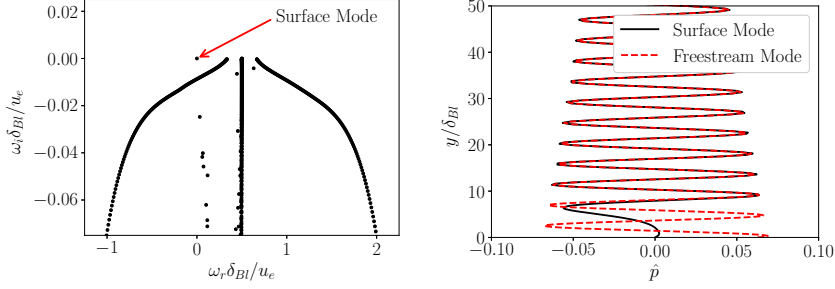


Figure 3: Eigenvalues (left) and surface mode pressure (right)

of sublimation occurring for each case is illustrated by the vapor mass fraction  $c_1$ , with the  $T_r = 1.2$  case consisting of 16% sublimated vapor at the wall. The case of  $T_r = 1.0$  corresponds to an adiabatic solid.

#### 4.1. Surface Mode Identification

The linearized governing equations with the quasi-steady conduction model are obtained for a given baseflow and the resulting temporal eigenvalue problem is solved. The eigenvalues near the origin for the  $T_r = 1.15$  baseflow are shown in Figure 3 with  $\alpha\delta_{Bl} = 0.5$ . Observe from Figure 3 that there is a single mode near the origin. This is the mode associated with surface recession (it appears only when recession effects are considered), and is herein called the “surface mode”. To show the characteristics of this mode, the Jacobian is transformed to primitive variables and the real part of the pressure component of the eigenvector is shown in the right panel of Figure 3. An overlay of the phase-aligned eigenvector for the uniform freestream system, provided in Özgen & Kırçalı (2008), is included for comparison. The oscillations observed in the freestream are a result of Mach waves with a wavenumber of

$$\alpha_y = \chi \cot\left(\sin^{-1}(1/M_n)\right), \quad (4.1)$$

where  $M_n$  is the normal Mach number. For the case analyzed in Figure 3, the Mach wave analysis predicts a wavenumber of  $\alpha_y\delta_{Bl} = 1.4142$  and the freestream eigenvalues predict a wavenumber of  $\alpha_y\delta_{Bl} = 1.4141$  with a decay rate of  $\alpha_y\delta_{Bl} = 0.0087$ .

#### 4.2. 2D Surface Modes

The temporal growth rates for 2D perturbations ( $\beta = 0$ ) were computed for a range of streamwise wavenumbers, and are presented in Figure 4. The results show that surface modes are unstable for wall temperatures exceeding the adiabatic case ( $T_r = 1.0$ ), with growth rates exhibiting a strong dependence on wall temperature. The stable results, from  $T_r \leq 1.0$ , are consistent with experimental observations that laminar flow gives stable surfaces. A critical wavenumber exists at which the temporal growth rate reaches a maximum for all cases, suggesting that a characteristic surface pattern with a specific wavelength may emerge on sublimating plates. For the  $T_r = 1.2$  case, the critical wavelength is approximately 22 mm. The wavelength correlation for crosshatch patterns provided in (Swigart 1974) for turbulent flows predicts a critical streamwise wavelength of 30 mm under the present freestream conditions. The approximate agreement between laminar and turbulent wavelengths is encouraging and possibly suggests a common underlying mechanism governing the critical wavenumber.

These results confirm the existence of a surface instability in flow over a sublimating surface, consistent with the findings of Lees *et al.* (1972). However, this is the first time such



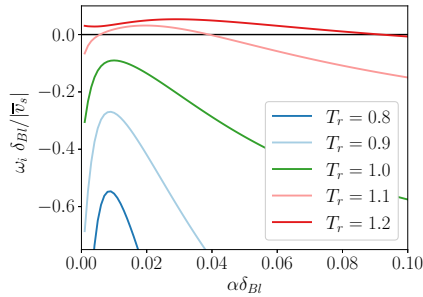


Figure 4: Growth rates for 2D surface modes. The black line marks neutral stability.

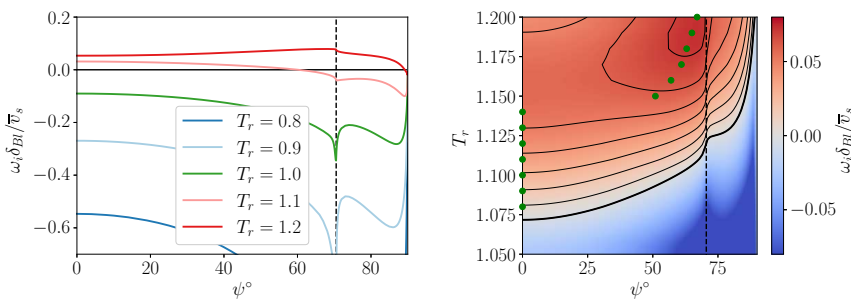


Figure 5: Oblique surface growth rates at  $\chi_{max}$  for select  $T_r$  (left) and at  $\chi_{max}$  for  $T_r = 1.05 - 1.2$  (right). The dashed lines mark the sonic angle,  $\psi_s$ . The thick solid black line marks neutral stability, while the thin black lines are iso-contours in 0.01 increments. The green dots mark the location of peak growth rate for each  $T_r$ , in 0.01 increments.

an instability has been identified in a laminar boundary layer, with the necessary condition of a hot wall ( $T_r > 1.0$ ). We hypothesize that the sign of the solid wall temperature gradient plays a crucial role in the surface stability by influencing the phase relationship between surface temperature fluctuations and surface position through the interface energy balance.

### 4.3. Oblique Surface Modes

Surface modes for oblique ( $\beta \neq 0$ ) perturbations were computed across a range of oblique angles, defined as  $\psi = \tan^{-1}(\beta/\alpha)$ , at the streamwise wavenumbers corresponding to the maximum 2D growth rate,  $\chi_{max}$ . The temporal growth rates are presented in Figure 5. The angle at which the normal Mach number reaches the sonic condition is indicated by the vertical dashed lines in Figure 5, and is given by  $\psi_s = \cos^{-1}(1/M_e)$ . This angle is also the complement of the Mach angle. The results in Figure 5 show that the 2D mode is the most unstable until  $T_r > 1.14$ , beyond which an oblique mode near the sonic angle becomes more unstable. The rapid transition of the most unstable orientation from 2D to oblique suggests the presence of two distinct instability mechanisms: one at  $\psi = 0$  and another near  $\psi = \psi_s$ . As the oblique angle increases across the sonic angle, the flow normal to the surface perturbation transitions from supersonic to subsonic and a sharp transition is observed in the temporal growth rates. As the oblique angle approaches  $90^\circ$  the normal Mach number drops to zero and the surface modes approach neutral stability.

## 5. Conclusion

The formulation for local linear stability analysis of sublimating surfaces is presented for a compressible boundary layer over a camphor plate. Temporal stability analysis is performed on sublimating baseflows, where hot walls were found to destabilize the laminar surface mode. The critical wavenumber corresponding to the maximum growth rate aligns with experimental observations of crosshatching wavelengths in turbulent flows. Our analysis also suggests that two-dimensional (i.e., spanwise-constant) surface modes are most unstable when  $T_r \leq 1.14$ , while three-dimensional modes are most unstable when  $T_r > 1.14$ . The developed linear stability framework can be used to investigate surface instabilities, which may be used to explain the formation of crosshatching. Future work may explore the effects of turbulent baseflows and other instability mechanisms such as inelastic deformation.

**Funding.** This work was supported by the LDRD Program at Sandia National Laboratories. Sandia is managed and operated by NTESS under DOE NNSA contract DE-NA0003525.

**Declaration of interests.** The authors report no conflict of interest.

## REFERENCES

- DORRANCE, WILLIAM H 1962 *Viscous hypersonic flow: theory of reacting and hypersonic boundary layers*. Courier Dover Publications.
- GHAFFARI, SHIRIN, MARXEN, OLAF, IACCARINO, GIANLUCA & SHAQFEH, ERIC 2010 Numerical simulations of hypersonic boundary-layer instability with wall blowing. In *48th AIAA Aerospace Sciences Meeting Including the New Horizons Forum and Aerospace Exposition*, p. 706.
- GRABOW, RM & WHITE, CO 1975 Surface roughness effects nosetip ablation characteristics. *AIAA journal* **13** (5), 605–609.
- HIRSCHFELDER, JOSEPH O, CURTISS, CHARLES F & BIRD, R BYRON 1964 *The molecular theory of gases and liquids*. John Wiley & Sons.
- KIM, SUN UNG & MONROE, CHARLES W 2014 High-accuracy calculations of sixteen collision integrals for lennard-jones (12–6) gases and their interpolation to parameterize neon, argon, and krypton. *Journal of Computational Physics* **273**, 358–373.
- LEES, LESTER, KUBOTA, TOSHI & KO, DENNY RS 1972 Stability theory for cross hatching part 1. linear stability theory. *Tech. Rep.*. SAMSO TR 72-34.
- LEKODIS, SPYRIDON G, NAYFEH, ALI H & SARIC, WILLIAM S 1976 Compressible boundary layers over wavy walls. *The physics of Fluids* **19** (4), 514–519.
- LYSENKO, VI, GAPONOV, SA, SMORODSKY, BV, KOSINOV, AD & YAROSLAVTSEV, MI 2021 Influence of surface sublimation on the stability of the supersonic boundary layer and the laminar–turbulent transition. *Physics of Fluids* **33** (2).
- ÖZGEN, SERKAN & KIRCALI, SENEM ATALAYER 2008 Linear stability analysis in compressible, flat-plate boundary-layers. *Theoretical and Computational Fluid Dynamics* **22**, 1–20.
- PADOVAN, ALBERTO, VOLLMER, BLAINE, PANERAI, FRANCESCO, PANESI, MARCO, STEPHANI, KELLY A & BODONY, DANIEL J 2024 An extended B' formulation for ablating-surface boundary conditions. *International Journal of Heat and Mass Transfer* **218**, 124770.
- STOCK, HANS W & GINOUX, JEAN J 1973 Hypersonic low temperature ablation an experimental study of cross-hatched surface patterns. In *Astronautical Research 1971: Proceedings of the 22nd Congress of the International Astronautical Federation Brussels, 20–25 September 1971*, pp. 105–120. Springer.
- STOCK, HANS W & GODDARD, M 1973 Cross-hatching: A comparison between behaviour of liquifying and sublimating ablation materials. *Tech. Rep.*. Von Karman Institute for Fluid Dynamics.
- SWIGART, RUDOLPH J 1974 Cross-hatching studies—a critical review. *AIAA Journal* **12** (10), 1301–1318.
- ZIBITSKER, ALEKSANDER L, MCQUAID, JOEL A, BREHM, CHRISTOPH & MARTIN, ALEXANDRE 2024 Validation and analysis of a coupled fluid-ablation framework for modeling low-temperature ablator. *International Journal of Heat and Mass Transfer* **218**, 124728.